Scripta Materialia 157 (2018) 62–66

Contents lists available at ScienceDirect

Scripta Materialia

journal homepage: www.elsevier.com/locate/scriptamat

Regular article

Elemental segregation to antiphase boundaries in a crept CoNi-based single crystal superalloy

Surendra Kumar Makineni [a,*], Malte Lenz [b], Steffen Neumeier [c], Erdmann Spiecker [b], Dierk Raabe [a,*], Baptiste Gault [a,*]

[a] Max-Planck-Institut für Eisenforschung GmbH, 40237 Düsseldorf, Germany
[b] Institute of Micro- and Nanostructure Research & Center for Nanoanalysis and Electron Microscopy (CENEM), Friedrich-Alexander-Universität Erlangen-Nürnberg, Cauerstraße 6, 91058 Erlangen, Germany
[c] Institute I: General Materials Properties, Friedrich-Alexander-Universität Erlangen-Nürnberg, Martensstr. 5, 91058 Erlangen, Germany

ARTICLE INFO

Article history:
Received 31 May 2018
Received in revised form 13 July 2018
Accepted 31 July 2018
Available online xxxx

Keywords:
Superalloys
Planar Defects
Antiphase Boundaries
Stacking Faults
Atom Probe Tomography

ABSTRACT

We report on the full three-dimensional compositional partitioning among the features of a planar imperfection comprising a superlattice intrinsic stacking fault (SISF) with its leading and trailing partials, as well as the antiphase boundary (APB) in the wake of the trailing partial formed in the $L1_2$-ordered γ′ phase of a CoNi-based single crystal superalloy. The partial dislocations and the APB are found to be Cr/Co rich relative to the surrounding γ′ and richer in W/Ta/Ti compared to the γ matrix phase. Solute diffusion mechanisms are derived from the compositional gradients in the vicinity of the imperfection.

Antiphase boundaries (APBs) are among the most common planar crystalline defects in γ/γ′ based superalloys [1] and are related to an anomalous positive flow stress behavior at high temperatures [2,3]. The γ matrix is a face-centered-cubic (fcc) disordered solid solution in which the $L1_2$-ordered γ′ phase precipitates are coherently embedded. In Ni-based alloys, APBs are present between two strongly coupled a/2 ⟨110⟩ superpartial dislocations gliding on {111} planes through γ′ during creep deformation at temperatures above 850 °C [4–6]. Their energy determines both, the threshold stress for γ′ cutting and the spacing among the superpartials. Hence, the APB energy is a crucial quantity that governs the alloy's high-temperature mechanical behavior [1,7–10].

The γ/γ′ microstructure was also discovered recently in Co- and CoNi-based alloys [11–14]. The CoNi-based γ/γ′ alloys [15–17] were shown to deform by the formation of APBs, however, with an a/2 ⟨112⟩ shear mechanism [17]. Additionally, it was shown that the formation of SISFs and APBs involves local reordering and chemical segregation driven by the reduction of the SISF [18] and APB energies [17] according to Gibbs. The APBs were shown to be enriched in Co/Cr, both γ stabilizers, relative to the surrounding γ′ lattice [17]. Similarly, in Ni-based superalloys, a few experimental reports show that γ stabilizing solutes segregate to the APBs [19–22]. This phenomenon was regarded as "wetting" of APBs [23,24] with the disordered γ phase, which was first reported in a Fe—Al based alloy by Swan et al. [25] and Allen et al. [26]. In CoNi-based superalloys, by utilizing an in-situ heating approach [17], it was also shown that the APB composition approaches that of the corresponding disordered γ phase, resulting in fragmentation of the γ′ precipitate. The growth and coarsening of APBs involve solute diffusion and, therefore, their respective rates depend on the diffusivities of the various solutes. However, quantitative measurements of the local diffusion and associated mechanisms occurring during high-temperature deformation have not been reported yet. Unveiling and explaining these mechanisms will help the design of novel alloys.

Until now, local chemical compositions of such types of microstructures were analyzed mainly by means of energy dispersive X-ray spectroscopy (EDXS) in transmission electron microscopes (TEM) operated in STEM mode [18,27,28]. When using STEM imaging, projection effects cannot be avoided and the sensitivity and quantification, especially for minor alloying elements can be limited. Here, we quantify the compositional partitioning among all of the constituting features of a planar imperfection comprising a SISF, the two bounding partial dislocations and the APB in three-dimensions with the aid of correlative atom probe tomography (APT) and electron microscopy. The imperfection was formed upon creep in the ordered γ′ phase of a new CoNi-based single crystal superalloy. The compositional gradients derived

* Corresponding authors.
E-mail addresses: sk.makineni@mpie.de (S.K. Makineni), d.raabe@mpie.de (D. Raabe), b.gault@mpie.de (B. Gault).

https://doi.org/10.1016/j.scriptamat.2018.07.042
1359-6462/

from our analysis allow us to predict the diffusive processes occurring during creep.

A CoNi-based single crystal alloy, named ERBOCo-1, with the composition Co-32Ni-8Al-5 W-6Cr-2.5Ti-1.5Ta-0.1Hf-0.4Si was prepared by the Bridgman process. It was subject to a multi-step heat treatment, viz. 1280 °C/8 h + 1050 °C/5 h + 900 °C/16 h to achieve a uniform γ/γ′ microstructure. The γ′ volume fraction in the alloy is measured to be ~ 61% which was evaluated by image analysis using ImageJ software [29]. Tensile specimens were cut and crept at 850 °C for 380 h at an applied stress of 400 MPa acting along the [001] direction up to 4.6% plastic strain. Cross-section samples with their plane normal close to the [110] direction were cut and mechanically polished for further microstructural characterization.

The creep deformed microstructure was observed by controlled electron channeling contrast imaging (cECCI) revealing the location of crystal defects [30]. A Zeiss Merlin scanning electron microscope (Carl Zeiss SMT, AG, Germany) equipped with a Gemini-type field emission gun electron column was used to perform electron backscattered diffraction (EBSD) mapping followed by cECCI in the same region-of-interest. The operating accelerating voltage was 30 kV with a probe current 4 nA and a working distance of 6 mm during imaging. cECCI exploits information from EBSD orientation determination, combined with simulation of electron channeling pattern (ECP) for different sample tilts, which we obtained from the software TOCA (Tools for Orientation Determination and Crystallographic Analysis) [31]. TOCA enables to determine the accurate sample stage settings to orient the specimen so as to obtain backscattered electron imaging in strong two-beam conditions [32].

Atom probe specimens for correlative investigation by TEM and APT were fabricated using a dual beam SEM/focused-ion-beam (FIB) instrument (FEI Helios Nanolab 600) following the protocol described in reference [33]. Regions containing the defects of interest were extracted from the bulk and subsequently sliced and welded using in-situ Pt-deposition on the end of the arms of an electropolished halved TEM Mo-grid inserted in a dedicated holder [34]. Slices were then sharpened by FIB milling at 30 kV followed by a final cleaning procedure at 2 kV and 16 pA to remove severely damaged regions. Transmission electron microscopy (TEM) on individual APT specimens was carried out in a Phillips CM-20 operated at 200 kV. A Cameca Instrument Inc. LEAP™ 5000XR, equipped with a reflectron for enhanced mass-resolving capability, was used for compositional analysis. APT data was acquired in laser pulsing mode at a repetition rate of 125 kHz and a pulse energy of 50 pJ. The specimen's base temperature was maintained at 40 K and the target detection rate was set to be 5 ions detected every 1000 pulses. The software package IVAS 3.8.0 was used for data reconstruction and analysis.

Fig. 1 shows an overview cECC image of the tensile crept CoNi-based superalloy along the [110] viewing direction. The micrograph was acquired in a two-beam condition with $g = (00\bar{2})$, where g is the diffraction vector. A clear atomic density contrast reveals rafted γ′ along the tensile loading direction embedded in darker γ channels. The bright contrast in the rafted γ′ corresponds to typical stacking faults (SFs) with bright lines formed due to the intersection of SF planes and the sample surface, as visible in the inset (a). Near the γ/γ′ interface region, a feature appears with a bright contrast extending away from the stacking fault shown in inset (b) and bows upwards towards the interface. This feature resembles the observation of APBs by TEM reported by Eggeler et al. [17], indicating the presence of such defects in the present crept alloy. In the subsequent analysis, we show that these features are indeed APBs. The curvature of the feature occurs due to the migration of the APB habit plane from {111} to {100}, which results in a reduction in the APB area and minimizes its specific energy [35,36].

An APT specimen was prepared from the location delimited by the dashed golden line in Fig. 1. Prior to APT probing, the presence of planar imperfections was confirmed by TEM. Figs. 2(a–b) respectively show a brightfield (BF) and a darkfield (DF) image taken from a superlattice $L1_2$ spot along the [110] zone axis of the APT specimen. The BF image shows clear contrast of straight dark lines resembling SFs. The absence of fringe contrast indicates that these faults are observed nearly edge-on. The DF image taken with a (010) superlattice reflection shows the γ′ phase in bright contrast. Regions where the $L1_2$ ordering is not maintained appear dark. This holds true for the γ phase, APBs and the damaged outer shell of the APT tip. Subsequently, a low energy cleaning of the specimen in the FIB (5 kV, lower current of 8 pA) was carried out to remove the e-beam contamination from the surface prior to APT analysis. Fig. 2(c) shows the distribution of Cr (pink dots) and Co

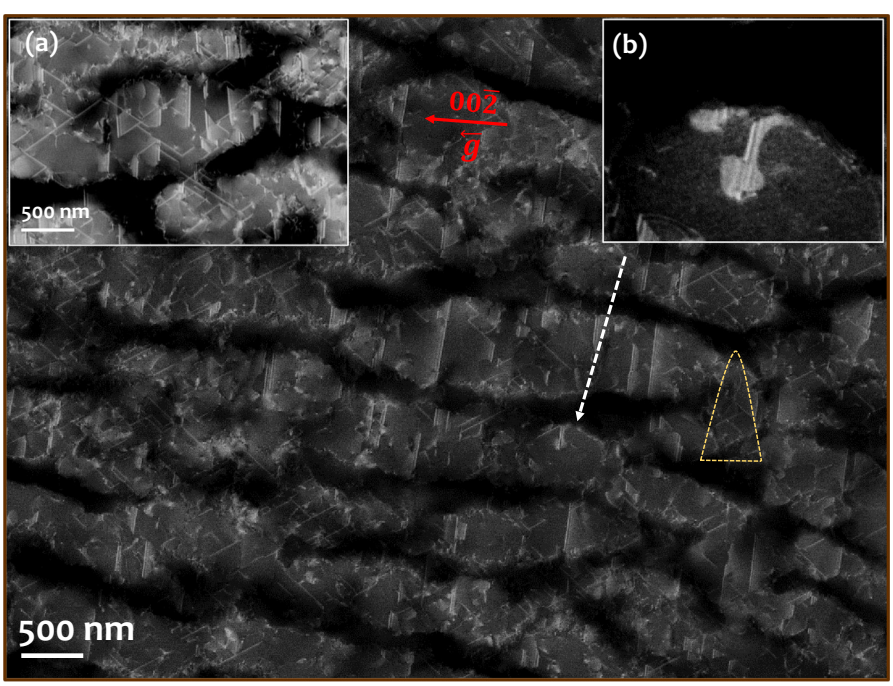

Fig. 1. An overview cECC image for the crept CoNi-based superalloy in two-beam diffraction condition ($g = (00\bar{2})$) showing a high number density of stacking faults (inset (a)) in the γ′ phase; inset (b) shows the bright contrast bowing upwards towards the γ/γ′ interface corresponding to an APB. (APB: Antiphase Boundary).

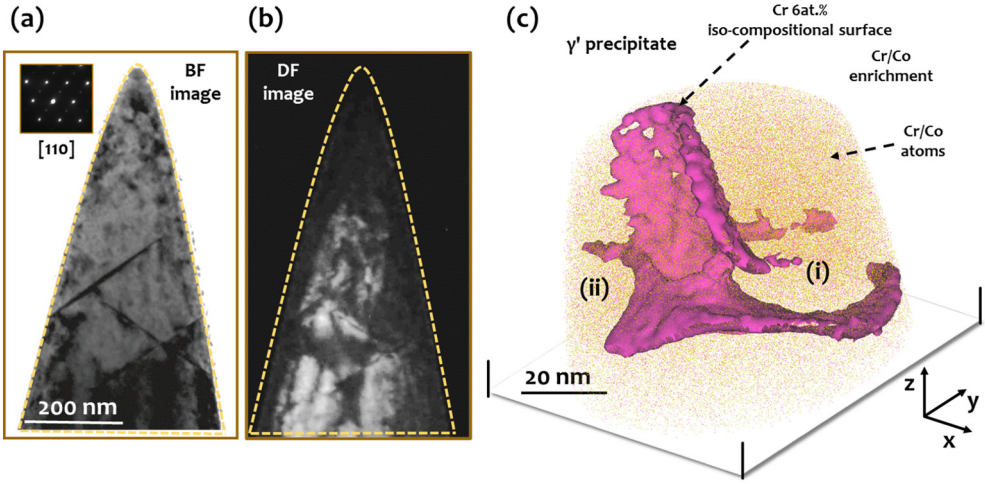

Fig. 2. (a) Brightfield (BF) image of an APT specimen taken near to [110] zone axis showing dark contrast lines corresponding to stacking faults in near edge-on view. (b) Darkfield (DF) image taken from the (010) superlattice spot reflecting the region with $L1_2$ ordering which shows that the tip contains mostly γ′ phase. (c) APT reconstruction showing the distribution of Cr (pink), Co (golden) atoms and their enrichment along certain features shown as a Cr 6 at.% iso-compositional surface (see also supplementary S1 and video V1). (For interpretation of the references to colour in this figure legend, the reader is referred to the web version of this article.)

(golden dots) atoms in an APT reconstruction evidencing a significant segregation of Cr and Co to different features (see supplementary Fig. S1). An iso-surface surrounding region in the point cloud locally containing >6 at.% Cr reveals curved boundaries as depicted in Fig. 2(c) and in the supplementary video V1. These Cr-rich boundaries form interconnected APBs and also reveal a linear Cr decoration (video V1), corresponding to segregation-enriched partial dislocations [37–39]. Two regions of interest were marked as (i) and (ii) in Fig. 2(c) where we will detail further analysis.

Fig. 3(a) shows a cut section of the region (i) rotated 180° around the x-axis (see the directional arrows). A 2D composition map for Al, obtained from the projection of the compositional field into the yz plane is also shown. This map reveals a confined Al-deficiency along a planar feature in-between two partial dislocations marked as the leading (LPD) and the curved trailing (TPD) partial dislocation. This planar feature corresponds to an SF. The TPD is followed by an APB in its wake that clearly bows out towards another orientation. The imaged imperfection is fully consistent with the schematic picture introduced by Eggeler et al. [17]. This involves a reaction of two different ½⟨101⟩ matrix dislocations at the γ/γ′ interface, producing a leading 1/3⟨112⟩ dislocation that shears through the γ′ creating a superlattice intrinsic stacking fault (SISF) leaving a trailing 1/6⟨112⟩ partial at the interface. Subsequently, the TPD enters into the γ′ precipitate, converting the SISF into an APB, and starts looping around with the simultaneous migration of the APB to the {100} planes. Fig. 3(b) shows the compositional profile perpendicular to the SISF plane depicted in Fig. 3(a) for Al, Cr, Ti, and Ta (see supplementary Fig. S2 for Co and Ni compositional profiles). At the SISF, the compositions of W and Co increase while Al and Ni deplete. We observe no notable compositional fluctuation of Cr, Ti, and Ta at the SISF. This observation is consistent with our earlier work [40] on the same alloy, also revealing such a confined depletion of Al/Ni along a plane that corresponds to a SISF. The measured compositions of the LPD and SISF are shown in Table 1.

Fig. 4 shows the magnified cut view of the region (ii) from Fig. 1(c) in the same orientation. A similar 2D compositional map of the Al distribution confirms the presence of a planar fault (a SISF) and its associated TPD with an APB behind. Supplementary Fig. S3 shows the additional compositional maps for W and Cr solutes revealing W enrichment confined to the SISF and Cr enrichment to the TPD and APB. Fig. 4(b) shows the distribution of Cr atoms viewed perpendicular to the projected Al compositional map in Fig. 4(a). The solute composition profiles along the fault plane were taken and shown in Fig. 4(c). The Cr composition is lower in the SISF region (~3.7 at.%) and increases to a value of ~11.9 at.% when crossing into the TPD. Subsequently, the composition drops to ~10.3 at.% and renders into a plateau. The W composition at the SISF is higher, while it drops at the TPD. Interestingly, a relative

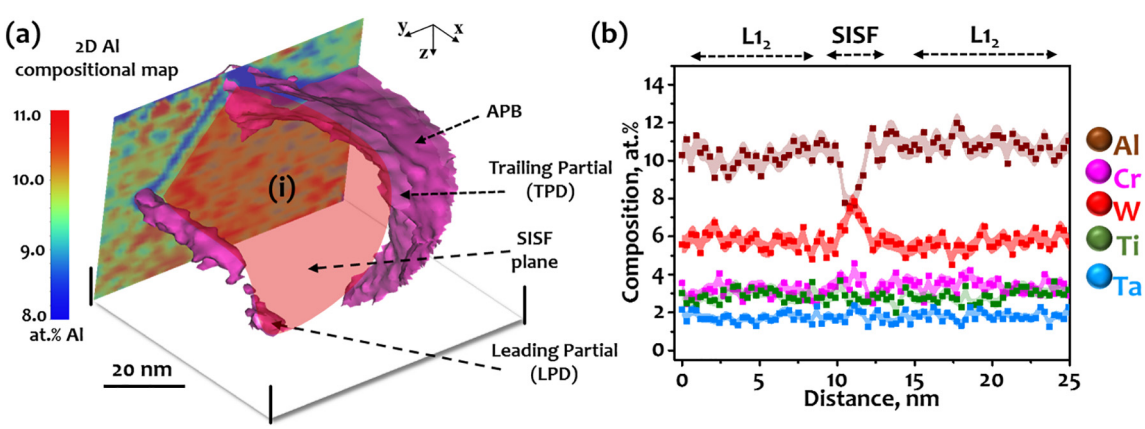

Fig. 3. (a) Joint 3D and 2D compositional presentation for solute Al projected along a plane, revealing presence and compositional decoration of a complex defect ensemble consisting of a leading partial dislocation (LPD), a superlattice intrinsic stacking fault (SISF), a trailing partial dislocation (TPD) and the APB (Antiphase Boundary). (b) Compositional profile perpendicular to the fault plane showing W (and Co in Supplementary Fig. S2) enrichment confined to the SISF embedded in the $L1_2$ lattice.

Table 1

Comparison of compositions in γ, γ′, LPD, SISF, TPD and APB in atomic percent (at.%). The error bar corresponds to the statistical error calculated as $\sigma = \sqrt{\frac{C_i(1-C_i)}{N}}$, where C_i is the composition of the solute species i and N is the total number of atoms in each bin. (LPD: Leading Partial Dislocation; SISF: Superlattice Intrinsic Stacking Fault; TPD: Trailing Partial Dislocation; APB: Antiphase Boundary).

	γ fcc matrix	γ′ $L1_2$ precipitate	Leading Partial Dislocation (LPD)	Stacking Fault (SISF)	Trailing Partial Dislocation (TPD)	Antiphase Boundary (APB)
Co	56.8 ± 0.2	40.8 ± 0.3	49.6 ± 1.3	46.2 ± 0.9	53.5 ± 1.5	49.9 ± 0.7
Ni	22.0 ± 0.3	35.2 ± 0.4	27.6 ± 1.2	29.2 ± 0.9	22.5 ± 1.4	25.4 ± 0.6
Cr	12.7 ± 0.1	3.6 ± 0.2	8.5 ± 0.7	3.7 ± 0.4	11.9 ± 0.9	10.3 ± 0.4
Al	4.1 ± 0.2	9.8 ± 0.3	5.6 ± 0.6	7.6 ± 0.5	4.8 ± 0.7	5.8 ± 0.3
W	3.0 ± 0.1	5.6 ± 0.2	5.2 ± 0.6	7.5 ± 0.5	4.2 ± 0.6	5.2 ± 0.3
Ti	0.95 ± 0.1	3.4 ± 0.1	1.9 ± 0.4	2.9 ± 0.2	1.4 ± 0.3	1.7 ± 0.2
Ta	0.4 ± 0.1	1.7 ± 0.2	0.9 ± 0.2	1.9 ± 0.3	0.7 ± 0.3	0.8 ± 0.1

pile-up of W solute was observed ahead of the TPD followed by a sudden drop and a subsequent plateau. The compositional profiles for Co, Ni along the fault plane and across the TPD and APB for all the solutes are shown in supplementary Figs. S4, S5, and S6 respectively.

The γ and γ′ compositions were also measured by APT. Supplementary Fig. S7 shows an APT reconstruction containing γ and γ′ with the composition profile across the γ/γ′ interface. The profile shows that the solutes Al, W, Ti, and Ta partition into the γ′ phase while Cr diffuses into the γ matrix phase, consistent with previous results obtained on quaternary and quinary Co-base superalloys [41,42]. The measured compositions for all the features are listed in Table 1.

The following important observations can be derived from our observations: 1) the APB is richer in W, Al, Ta and Ti with respect to the γ matrix composition; and 2) the leading and the trailing partial dislocations have different compositions. Our recent work [40] conducted by using correlative cECCI/TEM/APT investigations of a single SISF and its associated LPD evidenced a relative pileup of Al solute ahead of the LPD in the $L1_2$ lattice. In the present investigation, we observe a W pileup behind the TPD as shown in Fig. 4(c) and a higher composition of solutes at the APB with respect to the γ matrix. Combining these observations of solute pileups ahead of the LPD and behind the TPD, a corresponding diffusive mechanism during creep deformation at 850 °C, shown schematically in Fig. 4(d), is proposed: the solute pileup ahead of the LPD shows in-plane diffusion of Al/Ni from SISF towards the $L1_2$ lattice while W/Co diffuses in opposite direction and enriches at the SISF [40]. This selective solute migration is thermodynamically driven by the Gibbsian reduction in SISF energy [18]. These observations together with the W solute pile up behind the TPD shown in Fig. 4 (c) and the higher concentration of solutes inside the APB suggest that the diffusion of solutes (W, Al, Ta, and Ti) occurs in-plane towards the APB. More specifically, as the TPD moves, transforming the SISF into an APB, the solutes migrate to these boundaries. Further, as these boundaries are directly connected to the γ channels, the solutes tend to diffuse through these APBs simultaneously with the movement of TPD and LPD creating more APB area. This solute diffusion and the increased APB area result in the fragmentation of the γ′ phase and an associated loss of creep resistance. This assumption is supported by corresponding heating stage experiments [17] where it was shown that at high temperature (>1000 °C) the APBs coarsen and destabilize the γ′ phase. The difference in the LPD and TPD compositions can be attributed to the inequality in the magnitude of their associated Burgers vectors of both partial dislocations and hence their respective dislocation energies.

In conclusion, we show compositional variance among several planar and linear defect features including leading and trailing partial dislocations (LPD and TPD), superlattice intrinsic stacking fault (SISF),

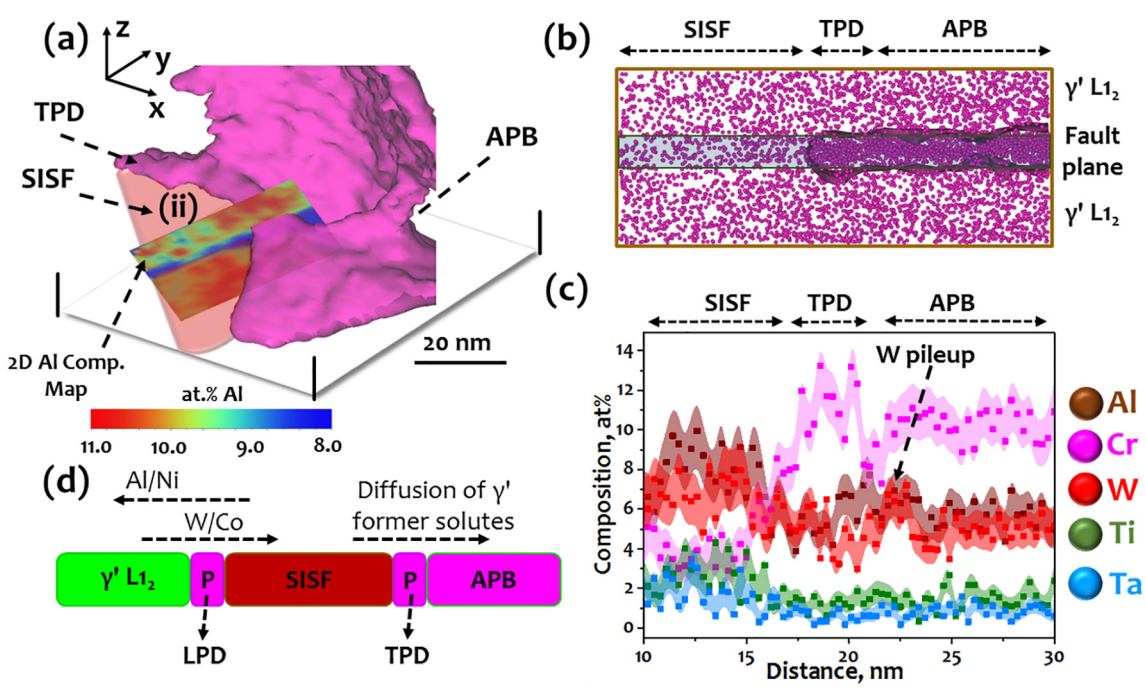

Fig. 4. (a) Analysis of the same data set shown in Fig. 2(c) revealing presence of another SISF, its associated TPD, and the connected APB in terms of joint 3D and 2D compositional concentration maps for Al in 3D space and also in a section along a plane across the planar fault. (b) Distribution of Cr atoms along the plane showing relative Cr enrichment confined to the LPD and APB. (c) Compositional profiles along the fault plane showing solute partitioning among SISF, TPD, and APB. (d) Schematic showing the planar defects features with the proposed solute diffusion directions. (LPD: Leading Partial Dislocation; SISF: Superlattice Intrinsic Stacking Fault; TPD: Trailing Partial Dislocation; APB: Antiphase Boundary).

and an antiphase boundary (APB) in a crept CoNi-based superalloy. The partial dislocations and the APB are Cr/Co enriched while the SISF is W/Co enriched with respect to the γ′ composition. The pileup of W solute behind the TPD shows that solute diffusion takes place towards the APB during creep-induced shearing of the γ′ phase.

Supplementary data to this article can be found online at https://doi.org/10.1016/j.scriptamat.2018.07.042.

Acknowledgments

The authors are grateful to U. Tezins and A. Sturm for their technical support of the atom probe tomography and focused ion beam facilities at the Max-Planck-Institut für Eisenforschung. SKM acknowledges financial support from the Alexander von Humboldt Foundation. The authors acknowledge financial support from the DFG SFB TR 103 through projects A1, A4, A7, and B3.

References

[1] R.C. Reed, The Superalloys: Fundamentals and Applications, Cambridge university press, 2008.
[2] P.H. Thornton, R.G. Davies, Metall. Mater. Trans. B Process Metall. Mater. Process. Sci. 1 (1970) 549–550.
[3] V. Paidar, D.P. Pope, V. Vitek, Acta Metall. 32 (1984) 435–448.
[4] R.C. Reed, N. Matan, D.C. Cox, M.A. Rist, C.M.F. Rae, Acta Mater. 47 (1999) 3367–3381.
[5] T.M. Pollock, A.S. Argon, Acta Metall. Mater. 40 (1992) 1–30.
[6] G.R. Leverant, B.H. Kear, J.M. Oblak, Metall. Trans. A. 4 (1973) 355–362.
[7] K.J. Hemker, M.J. Mills, Philos. Mag. A 68 (1993) 305–324.
[8] H.P. Karnthaler, E.T. Mühlbacher, C. Rentenberger, Acta Mater. 44 (1996) 547–560.
[9] A.T. Paxton, Y.Q. Sun, Philos. Mag. A 78 (1998) 85–104.
[10] D.M. Dimiduk, A.W. Thompson, J.C. Williams, Philos. Mag. A 67 (1993) 675–698.
[11] J. Sato, T. Omori, K. Oikawa, I. Ohnuma, R. Kainuma, K. Ishida, Science 312 (2006) 90–91.
[12] S.K. Makineni, B. Nithin, K. Chattopadhyay, Scr. Mater. 98 (2015) 36–39.
[13] S.K. Makineni, B. Nithin, K. Chattopadhyay, Acta Mater. 85 (2015) 85–94.
[14] S.K. Makineni, A. Samanta, T. Rojhirunsakool, T. Alam, B. Nithin, A.K. Singh, R. Banerjee, K. Chattopadhyay, Acta Mater. 97 (2015) 29–40.
[15] Y.M. Eggeler, M.S. Titus, A. Suzuki, T.M. Pollock, Acta Mater. 77 (2014) 352–359.
[16] M.S. Titus, Y.M. Eggeler, A. Suzuki, T.M. Pollock, Acta Mater. 82 (2015) 530–539.
[17] Y.M. Eggeler, J. Müller, M.S. Titus, A. Suzuki, T.M. Pollock, E. Spiecker, Acta Mater. 113 (2016) 335–349.
[18] M.S. Titus, A. Mottura, G. Babu Viswanathan, A. Suzuki, M.J. Mills, T.M. Pollock, Acta Mater. 89 (2015) 423–437.
[19] C.Y. Chen, R. Schäublin, W.M. Stobbs, Mater. Sci. Eng. A 360 (2003) 356–364.
[20] C.Y. Chen, W.M. Stobbs, Metall. Mater. Trans. A 35 (2004) 733–740.
[21] M. Sluiter, Y. Hashi, Y. Kawazoe, Comput. Mater. Sci. 14 (1999) 283–290.
[22] D. Barba, T.M. Smith, J. Miao, M.J. Mills, R.C. Reed, Metall. Mater. Trans. A (2018) 1–13.
[23] J.E. Krzanowski, S.M. Allen, Acta Metall. 31 (1983) 213–222.
[24] C. Leroux, A. Loiseau, M.C. Cadeville, D. Broddin, G.V. Tendeloo, J. Phys. Condens. Matter 2 (1990) 3479.
[25] P.R. Swann, W.R. Duff, R.M. Fisher, Metall. Mater. Trans. B Process Metall. Mater. Process. Sci. 3 (1972) 413–423.
[26] S.M. Allen, J.W. Cahn, Acta Metall. 27 (1979) 1085–1095.
[27] G.B. Viswanathan, R. Shi, A. Genc, V.A. Vorontsov, L. Kovarik, C.M.F. Rae, M.J. Mills, Scr. Mater. 94 (2015) 5–8.
[28] T.M. Smith, B.D. Esser, N. Antolin, G.B. Viswanathan, T. Hanlon, A. Wessman, D. Mourer, W. Windl, D.W. McComb, M.J. Mills, Acta Mater. 100 (2015) 19–31.
[29] N. Volz, C.H. Zenk, R. Cherukuri, T. Kalfhaus, M. Weiser, S.K. Makineni, C. Betzing, M. Lenz, B. Gault, S.G. Fries, J. Schreuer, R. Vaßen, S. Virtanen, D. Raabe, E. Spiecker, S. Neumeier, M. Göken, Metall. Mater. Trans. A (2018) 1–11.
[30] S. Zaefferer, N.-N. Elhami, Acta Mater. 75 (2014) 20–50.
[31] I. Gutierrez-Urrutia, S. Zaefferer, D. Raabe, JOM 65 (2013) 1229–1236.
[32] S. Zaefferer, S. Kleindiek, K. Schock, B. Volbert, Microsc. Microanal. 19 (2013) 1306–1307.
[33] S.K. Makineni, M. Lenz, P. Kontis, Z. Li, A. Kumar, P.J. Felfer, S. Neumeier, M. Herbig, E. Spiecker, D. Raabe, B. Gault, JOM (2018) 1–8.
[34] M. Herbig, P. Choi, D. Raabe, Ultramicroscopy 153 (2015) 32–39.
[35] R. Kikuchi, J.W. Cahn, Acta Metall. 27 (1979) 1337–1353.
[36] J.A. Horton, C.T. Liu, Acta Metall. 33 (1985) 2191–2198.
[37] M. Kuzmina, M. Herbig, D. Ponge, S. Sandlöbes, D. Raabe, Science 349 (2015) 1080–1083.
[38] A. Kwiatkowski Da Silva, G. Leyson, M. Kuzmina, D. Ponge, M. Herbig, S. Sandlöbes, B. Gault, J. Neugebauer, D. Raabe, Acta Mater. 124 (2017) 305–315.
[39] A.K. da Silva, D. Ponge, Z. Peng, G. Inden, Y. Lu, A. Breen, B. Gault, D. Raabe, Nat. Commun. 9 (2018) 1137.
[40] S.K. Makineni, A. Kumar, M. Lenz, P. Kontis, T. Meiners, C. Zenk, S. Zaefferer, G. Eggeler, S. Neumeier, E. Spiecker, D. Raabe, B. Gault, Acta Mater. 155 (2018) 362–371.
[41] I. Povstugar, P.-P. Choi, S. Neumeier, A. Bauer, C.H. Zenk, M. Göken, D. Raabe, Acta Mater. 78 (2014) 78–85.
[42] I. Povstugar, C.H. Zenk, R. Li, P.-P. Choi, S. Neumeier, O. Dolotko, M. Hoelzel, M. Göken, D. Raabe, Mater. Sci. Technol. 32 (2016) 220–225.